Universal instabilities of radio-frequency traps

I. Garrick-Bethell,[1] Th. Clausen,[2] and R. Blümel[2]
[1]*MIT Center for Space Research, Cambridge, Massachusetts 02139, USA*
[2]*Department of Physics, Wesleyan University, Middletown, Connecticut 06459-0155, USA*
(Received 3 September 2003; published 26 May 2004)

Using standard tools of nonlinear dynamics we analyze recently discovered instabilities of radio-frequency charged-particle traps. In the cw-driven cylindrical Kingdon trap the instabilities occur at the two values $\eta_3^*=3.613\,046\,7\ldots$ and $\eta_4^*=4.431\,124\,4\ldots$ of the trap's control parameter η. Analytical estimates based on the theory of Mathieu functions predict $\eta_3^*=\pi\sqrt{(363-32\pi^2)/(66\pi\sqrt{6}-48\pi^2)}=3.692\,392\,2\ldots$ and $\eta_4^*=(\sqrt{\pi}/2)\times[(363-32\pi^2)/(\sqrt{1089+48\pi^2}-12\pi)]^{1/2}=4.496\,546\,6\ldots$. The kicked Kingdon trap, an analytically solvable model, predicts $\eta_3^*=\frac{1}{3}\sqrt{105}=3.415\,650\,2\ldots$ and $\eta_4^*=\sqrt{17}=4.123\,105\,6\ldots$. We show that similar instabilities occur in the two-particle Paul trap and the cw-driven spherical Kingdon trap.

DOI: 10.1103/PhysRevE.69.056222 PACS number(s): 05.45.−a, 32.80.Pj

I. INTRODUCTION

One of the most fruitful ideas of modern physics is the isolation and levitation of a countable number of charged particles in electromagnetic traps [1]. An important class of charged-particle traps are the radio-frequency traps. Its most celebrated member, the Paul trap [2], was invented in the 1950s [3] and is still one of the most important laboratory tools for the trapping of atomic and subatomic charged particles. A quick search of the database INSPEC revealed that over the past five years no fewer than 200 papers were published on the Paul trap and its applications in fields ranging from squeezed states [4,5] and cavity quantum electrodynamics [6] to novel frequency standards [7,8] and quantum information processing [9,10]. Radio-frequency (rf) traps primarily suited for the experimental and theoretical investigation of nonlinear dynamics are the cylindrical [11–13] and the spherical [13,14] dynamic Kingdon traps. Since rf traps are indispensable tools in countless physics laboratories throughout the world, it is important to know their properties. With the exception of the ideal single-particle Paul trap, which is integrable both classically and quantum mechanically [15,16], all rf traps are conceptually equivalent: they are periodically driven nonlinear oscillators. In many cases, especially if only a few particles are stored simultaneously in the traps, it is possible to describe the trapped particles' dynamics by two-dimensional area-preserving mappings. These mappings exhibit universal properties [17,18] such as bifurcations and low-order resonances which point to the possible existence of dangerous universal instabilities of rf traps. Indeed we recently found two pronounced instabilities of the cylindrical dynamic Kingdon trap [19,20] which can be traced back to well-known low-order resonances and bifurcations of two-dimensional area-preserving maps [17,18]. We emphasize that the instabilities discussed in this paper have nothing to do with the well-known instabilities caused by field defects resulting in nonlinear coupling between different degrees of freedom [21,22]. The instabilities discussed in this paper are single-degree-of-freedom dynamic instabilities of the ideal traps which can be explained as due to universal instabilities of the associated area-preserving maps [17,18].

The purpose of this paper is to analyze the particle dynamics in rf traps using standard techniques of nonlinear dynamics and to predict the existence of experimentally verifiable instabilities in the Paul trap and the two dynamic Kingdon traps. Knowledge of these instabilities is of utmost importance for successfully operating these traps in the laboratory.

The plan of this paper is as follows. In Sec. II we start with a detailed analysis of the cylindrical dynamic Kingdon trap. We chose this trap as the starting point of our presentation because it has only a single control parameter and its dynamics is already nonlinear for a single stored particle. This fact allows a particularly clear exposition and the direct application of standard nonlinear dynamics tools. In Sec. III we present the kicked dynamic Kingdon trap. We show that the kicked trap is an excellent model for the cw-driven dynamic Kingdon trap. Moreover, due to the impulsive drive of this trap, its dynamics is exactly described by an area-preserving two-dimensional mapping whose instabilities can be computed analytically. They are shown to agree well with the exact instability points of the cw-driven trap. In Secs. IV and V we show that the instabilities we found in the cylindrical dynamic Kingdon trap are universal in the sense that they also manifest themselves in the spherical dynamic Kingdon trap (Sec. IV) and the Paul trap (Sec. V). In Sec. VI we discuss our results. In Sec. VII we summarize our results and conclude the paper. In the Appendix we present a high-accuracy approximation of the limit cycle of the cylindrical dynamic Kingdon trap which may be used in future investigations for a more accurate analytical calculation of the predicted instabilities of the cw-driven cylindrical dynamic Kingdon trap.

II. CYLINDRICAL DYNAMIC KINGDON TRAP

The Kingdon trap [23,24] is the tool of choice for the investigation of topics ranging from laboratory models of the solar system [25] to the precise measurement of the lifetimes of metastable levels of heavy ions [26]. A variant of the Kingdon trap, the dynamic Kingdon trap [11,12], is the focus of this section. As shown in Fig. 1 the hardware of this trap

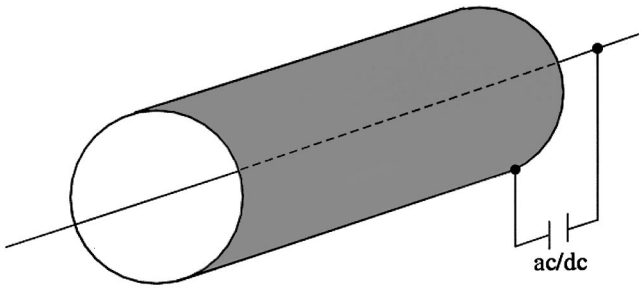

FIG. 1. Sketch of the cylindrical dynamic Kingdon trap. A superposition of ac and dc voltages is applied between a rectilinear wire and a surrounding cylindrical conductor resulting in dynamical trapping of a charged particle in the free space between the wire and the cylinder.

is of stunning simplicity. In principle the trap consists of nothing more than a rectilinear wire surrounded by a conducting cylindrical surface with a superposition of ac and dc voltages applied between them. Its simple design notwithstanding, the classical dynamics of a particle stored in the dynamic Kingdon trap is nonlinear [11,12,27] and exhibits many of the properties of classically chaotic systems [11,12,27,28].

Historically the cylindrical dynamic Kingdon trap was first investigated at Freiburg University [29,30], where it was used as a mass-selective ion source. The results of this investigation, however, were never published in the open literature [31]. In Ref. [11] this trap was rediscovered and proposed as a convenient microlaboratory for the investigation of classical and quantum chaos [28] and ion crystallization [12].

For the past eight years the nonlinear dynamics of the trap has been investigated in great detail both theoretically [11,12,14,27,32] and experimentally [13,33]. Therefore it came as a surprise when it was discovered only recently [19,20] that voltage settings exist which render the trap completely unstable. The detailed investigation of these instabilities is the focus of this section.

In Sec. II A we present the equation of motion of a charged particle in the dynamic Kingdon trap and, with the help of numerically computed phase-space portraits, explain qualitatively the trapping mechanism. In Sec. II B we present a detailed survey of the size of the primary trapping island of the dynamic Kingdon trap. This survey points to the existence of fundamental instabilities of the trap and yields numerical estimates for the critical values of the trap control parameter at which the instabilities occur. In Sec. II C we use Poincaré sections to reveal the origin of these instabilities: the complete collapse of the primary trapping island due to a collision between the trap's first-order fixed point and a set of third- or fourth-order fixed points. A resonance mechanism, well known in the theory of two-dimensional area-preserving mappings [17,18], allows us in Sec. II D to compute the critical values of the trap's control parameter numerically with high precision and to obtain accurate analytical estimates. In Sec. II E we establish a connection between the instabilities of the dynamic Kingdon trap and general results in the theory of two-dimensional area-preserving mappings.

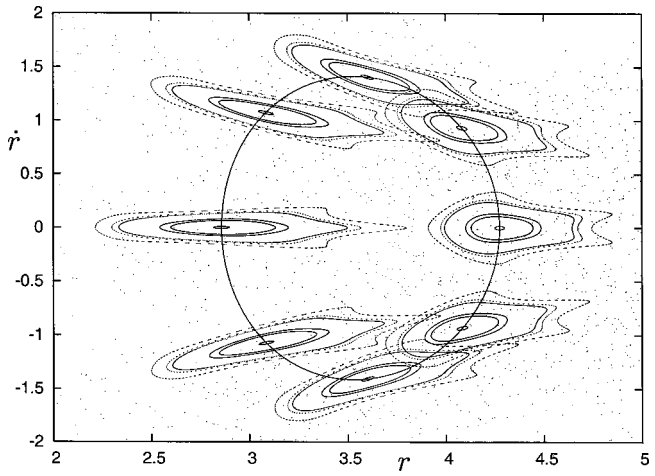

FIG. 2. Multiple-exposure Poincaré section for $\eta=5$ illustrating the organization of the phase space of the dynamic Kingdon trap around its limit cycle (full line).

A. Working principle of the dynamic Kingdon trap

The dimensionless equation of motion of a charged particle in the electric field of the dynamic Kingdon trap is given by [11]

$$\frac{d^2r}{dt^2} = -[1 - 2\eta\cos(2t)]\frac{1}{r}, \tag{1}$$

where t is dimensionless time, r is the dimensionless distance of the particle from the wire, and η is the dimensionless control parameter. For $\eta > \eta_1 \approx 3.125$ (1) has a π-periodic solution $r_L(t)$, i.e., a limit cycle [34]. A good approximation for $r_L(t)$ is given by (see Ref. [11] and the Appendix)

$$r_L(t) \approx \frac{\eta}{\sqrt{2}} - \frac{1}{\sqrt{2}}\cos(2t). \tag{2}$$

For a generic choice of $\eta > \eta_1$ the limit cycle $r_L(t)$ is stable. As an example we computed the limit cycle for $\eta=5$. It is shown as the full line in Fig. 2. At $\eta=\eta_1$ the limit cycle $r_L(t)$ undergoes a period-doubling bifurcation with further bifurcations at $\eta_2 \approx 2.938$, $\eta_3 \approx 2.917, \ldots$ [11]. The period-doubling scenario for $\eta \leqslant \eta_1$ has already been investigated in detail [11,27]. This is why in this paper we focus our investigation of Eq. (1) on the range $\eta \geqslant 3$, which includes η_1 but none of the other bifurcation points.

In order to gain further insight into the working principle of the dynamic Kingdon trap, we investigate its phase-space structure. Phase space is explored with the help of phase-space portraits. They are produced by turning Eq. (1) into a mapping

$$M_\tau(\eta): [r(t), \dot{r}(t)] \mapsto [r'(t+\tau), \dot{r}'(t+\tau)]. \tag{3}$$

The mapping (3) is called a "stroboscopic mapping" since it is constructed by examining the solutions of Eq. (1) at regularly spaced "snapshots" a time interval τ apart. Usually τ is chosen to be equal to the period of Eq. (1), i.e., $\tau=\pi$. In this case the mapping (3) is invertible and we identify

$$M_\pi(\eta) \equiv M(\eta). \tag{4}$$

Occasionally, however, other strobing times τ turn out to be useful (see discussion below).

As a first application of the stroboscopic mapping (3) we show that the phase-space dynamics of Eq. (1) is organized around $r_L(t)$. This is demonstrated in Fig. 2 by means of a "multiple-exposure" Poincaré section produced on the basis of Eq. (3) with $\tau=\pi/8$ in the following way. We solve Eq. (1) for 121 different initial conditions $(r_m,\dot{r}_n)=[2+(m-1)0.3,-2+(n-1)0.4]$, $m,n=1,\ldots,11$, and strobe the resulting phase-space trajectories at $t_k^{(j)}=k\pi+(j-1)\pi/8$, $k=1,\ldots,500$, $j=1,\ldots,8$. Figure 2 shows that for each j we obtain an island of stability organized around the limit cycle $r_L(t)$. This explains the trapping mechanism of a charged particle in the dynamic Kingdon trap. Started at $t=0$, somewhere in the leftmost island of stability, the phase-space trajectory of the particle is carried clockwise along the limit cycle from one stable island to the next. As a result, the particle is trapped forever, but executes an oscillatory motion in both r and $\dot{r}$, which is known as its *micromotion* [35]. If a particle is launched outside of the stable island in the chaotic sea, it will, for some time, follow a transiently chaotic trajectory until it hits the wire or the cylinder, discharges, and falls out of the trap.

The stable phase-space island whose center is pierced by the limit cycle is called the *primary trapping island*. Since Eq. (1) is nonlinear, there exist, in general, secondary trapping islands surrounding the primary trapping island. These islands, however, are generally smaller than the large primary trapping island, and not of much practical importance for trapping.

B. Trapping efficiency

Trapping in the dynamic Kingdon trap is a nonlinear effect which depends decisively on the existence of stable islands in phase space. In this respect the dynamic Kingdon trap is fundamentally different from the Paul trap [1–3] or the Penning trap [36], in which, in principle, particles can be stored irrespective of their positions and momenta. We define the sum-total $S(\eta)$ of all stable phase-space areas of Eq. (1) as the *trapping efficiency* of the dynamic Kingdon trap for control parameter setting η. Since, as mentioned above, secondary islands are usually much smaller than the primary trapping island, $S(\eta)$ is also a good approximate measure of the phase-space area of the primary trapping island.

In order to compute S as a function of η we computed 701 stroboscopic Poincaré sections (strobing times $t_k=k\pi$, $k=1,\ldots,1000$) of Eq. (1) for η values ranging from $\eta=3$ to $\eta=10$ in steps of $\delta\eta=0.01$ and determined the stable phase-space areas numerically with a phase-space resolution $\Delta r\times\Delta\dot{r}$ of better than 2×10^{-4}. The result is shown in Fig. 3(a). We see that from about $\eta=4.5$ on $S(\eta)$ is positive and increasing on average. This means that in this η regime the dynamic Kingdon trap provides stable trapping of charged particles. However, as shown by the inset of Fig. 3(a), $S(\eta)$ vanishes twice in the interval $3<\eta<4.5$ at two critical control parameters, which we call η_3^* and η_4^*. On the basis of our

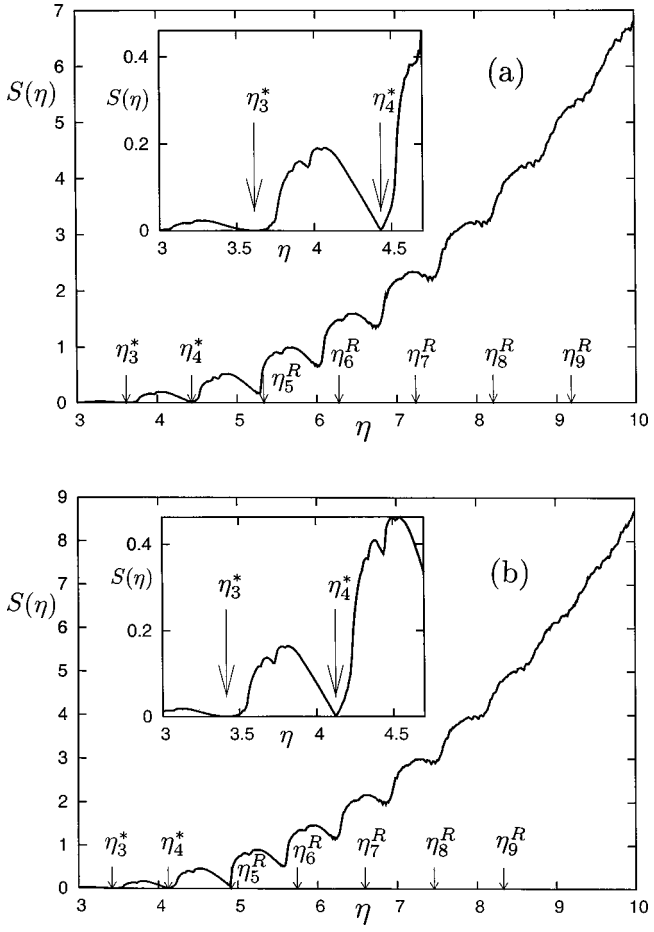

FIG. 3. The stability function S, a measure of the phase-space area of stable islands, as a function of the control parameter η for the cw-driven trap (a) and the kicked trap (b). The insets show that for both traps $S(\eta)$ vanishes twice in the interval $3\leqslant\eta\leqslant10$ at η values, called η_3^* and η_4^* (marked by arrows), indicating complete instability of the traps at these critical control parameters. The arrows at η_N^R, $N\geqslant5$, mark the η values where the rotation frequency of the center of the primary trapping island is in resonance with (a) the frequency of the trap's ac voltage and (b) the kick frequency of the trap.

η resolution of $\delta\eta=0.01$ we determined that $S(\eta)$ vanishes at

$$\eta_3^* \approx 3.61, \quad \eta_4^* \approx 4.43. \tag{5}$$

As is barely discernible from the inset of Fig. 3(a), but confirmed by additional detailed numerical calculations, $S(\eta)$ does not vanish at $\eta=\eta_1$, the location of the first bifurcation of the limit cycle. Thus η_3^* and η_4^* are indeed the only values in the range $3\leqslant\eta\leqslant10$ where $S(\eta)$ vanishes. A vanishing S means that no stable trapping is possible. Therefore the trap is unstable at η_3^* and η_4^*. A detailed examination of phase-space portraits presented in the following section will shed more light on the origin of these instabilities.

C. Island collapse

In this section we show that the instabilities of the trap at η_3^* and η_4^* are due to the complete collapse of the primary

trapping island of Eq. (1) at these two critical values of the trap's control parameter η. Inspecting many phase-space portraits of $M(\eta)$ in the vicinity of η_3^*, we found that as η approaches η_3^* a set of unstable period-3 fixed points move in on the center of the primary trapping island (a period-1 fixed point) squeezing the primary trapping island to zero phase-space area at $\eta=\eta_3^*$. A similar mechanism is at work in the vicinity of η_4^*. Here a set of unstable period-4 fixed points approaches the primary trapping island squeezing it to zero phase-space area at $\eta=\eta_4^*$. Close visual inspection of a large database of phase-space plots in the vicinity of η_3^* and η_4^* allowed us to improve the accuracy of Eq. (5). On the basis of our graphical material we determined that the primary trapping island shrinks to zero phase-space area at

$$\eta_3^* \approx 3.613, \quad \eta_4^* \approx 4.431. \tag{6}$$

These values are consistent with Eq. (5).

The island collapse mechanism discussed above is illustrated in Figs. 4 and 5. Figure 4 shows a sequence of three phase-space portraits for $\eta=3.57$ (a), $\eta=3.613\approx\eta_3^*$ (b), and $\eta=3.65$ (c). The three panels of Fig. 4 show that the size of the primary trapping island is entirely determined by the location of a set of unstable period-3 fixed points of the stroboscopic Poincaré mapping. As shown in Fig. 4, the primary island is indeed squeezed to zero area at η_3^* as the unstable period-3 fixed points move in to collide with the primary period-1 fixed point at η_3^*. The "triangle" defining the boundaries of the primary trapping island for η close to η_3^*, but $\eta\neq\eta_3^*$, is an example of a homoclinic cycle [34] formed of the degenerate stable and unstable manifolds of the unstable period-3 fixed points.

Figure 5 illustrates the collapse mechanism at η_4^*. As shown in Fig. 5, a set of collapsing period-4 fixed points squeeze the primary trapping island to zero phase-space area at $\eta=\eta_4^*$. The instability mechanism based on a collapsing set of unstable period-3 and period-4 fixed points explains our notation for the two critical η values.

D. Critical control parameters

As discussed in the preceding section, the reason for the instabilities of the trap at η_3^* and η_4^* is the caging of the primary trapping island by unstable, third- and fourth-order fixed points, respectively, which collapse to a point at the two critical control parameters. For η close to η_3^* a phase-space trajectory started at $t=0$ inside of the primary trapping island will have twisted by an angle of approximately $2\pi/3$ around the limit cycle $r_L(t)$ at $t=\pi$ owing to its proximity to the third-order fixed points. At $\eta=\eta_3^*$ the twist angle will be exactly $2\pi/3$ due to the fact that at η_3^* the center of the primary trapping island and the third-order fixed points are degenerate. This defines a resonance mechanism which we use to compute η_3^* and η_4^* according to the following procedure. We linearize (1) around $r_L(t)$ and determine η_3^* and η_4^* according to the condition that the twist angle of the linearized mapping equals $2\pi/3$ and $2\pi/4$, respectively. Defining

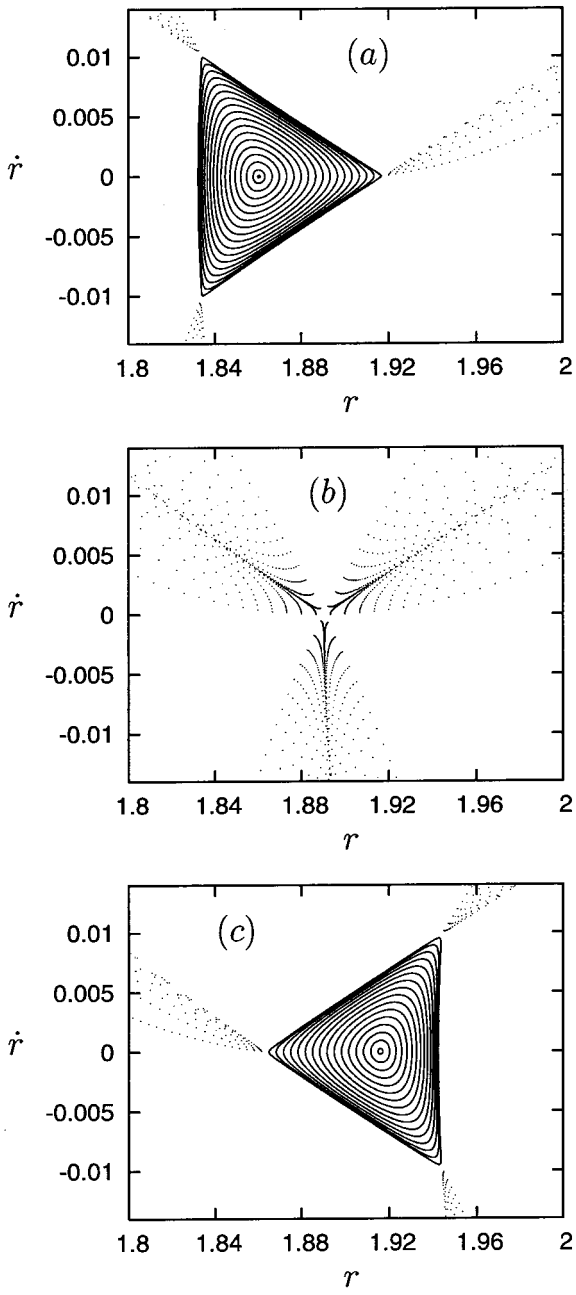

FIG. 4. Illustration of the collapse of the primary trapping island of the cylindrical dynamic Kingdon trap in the vicinity of $\eta=\eta_3^*$. (a) $\eta=3.57$, (b) $\eta=3.613\approx\eta_3^*$, (c) $\eta=3.65$. A set of unstable period-3 fixed points ($\eta<\eta_3^*$) (a) collapses at $\eta=\eta_3^*$ (b) squeezing the primary trapping island to zero phase-space area. The primary trapping island reemerges for $\eta>\eta_3^*$ (c).

$$r(t) = r_L(t) + \xi(t), \quad \dot{r}(t) = \dot{r}_L(t) + p(t), \tag{7}$$

we linearize Eq. (1), obtaining the following system of equations for $\xi(t)$ and $p(t)$:

$$\dot{\xi}(t) = p(t),$$

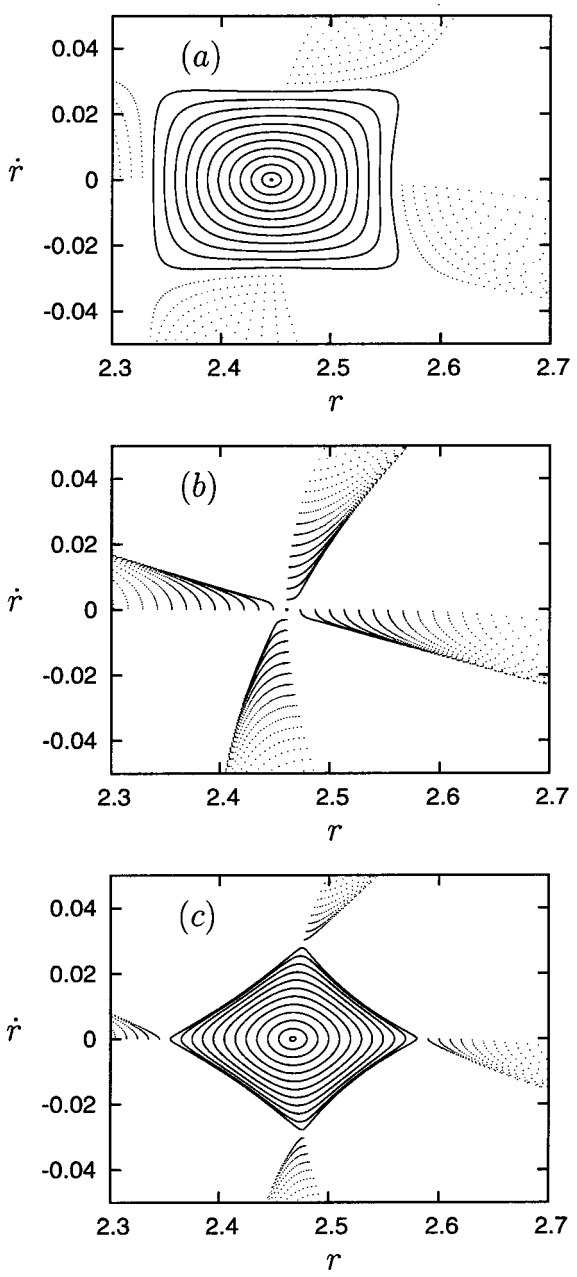

FIG. 5. Collapse of the primary trapping island of the cylindrical dynamic Kingdon trap in the vicinity of $\eta=\eta_4^*$. (a) $\eta=4.41$, (b) $\eta=4.431\approx\eta_4^*$, (c) $\eta=4.44$. A set of unstable period-4 fixed points ($\eta<\eta_4^*$) (a) collapses at $\eta=\eta_4^*$, (b) squeezing the primary trapping island to zero phase-space area. The primary trapping island re-emerges for $\eta>\eta_4^*$ (c).

$$\dot{p}(t)=\frac{1-2\eta\cos(2t)}{r_L^2(t)}\xi(t). \tag{8}$$

Integrating Eq. (8) from $t=0$ to $t=\pi$ defines the linearized one-cycle mapping

$$\begin{pmatrix}\xi'\\ p'\end{pmatrix}=\Lambda(\eta)\begin{pmatrix}\xi\\ p\end{pmatrix}, \tag{9}$$

where (ξ',p') are position and momentum at $t=\pi$ when starting with (ξ,p) at $t=0$. The matrix elements of Λ depend only on η and are determined by a two-step process in the following way. Starting with $\xi(0)=1$, $p(0)=0$, and integrating Eq. (8) over one cycle yields $\Lambda_{11}=\xi(\pi)$, $\Lambda_{21}=p(\pi)$. Starting with $\xi(0)=0$, $p(0)=1$ yields $\Lambda_{12}=\xi(\pi)$, $\Lambda_{22}=p(\pi)$. Since the primary trapping island is an elliptical island, the eigenvalues of $\Lambda(\eta)$ are of the form $\lambda_{1,2}(\eta)=\exp[\pm i\varphi(\eta)]$, where $\varphi(\eta)$ is the twist angle. Solving the equations $\varphi(\eta)=2\pi/3$ and $\varphi(\eta)=2\pi/4$ numerically yields

$$\eta_3^*=3.613\,046\,7\ldots,\quad \eta_4^*=4.431\,124\,4\ldots, \tag{10}$$

respectively. These values are consistent with Eq. (6).

The pronounced local minima in $S(\eta)$ for $\eta>\eta_4^*$ (see Fig. 3) can be explained qualitatively with the same mechanism that gave rise to the instabilities at η_3^* and η_4^*. The first pronounced minimum in $S(\eta)$ to the right of η_4^* is caused by a set of unstable period-5 fixed points caging the primary trapping island; the next minimum is caused by a set of unstable period-6 fixed points caging the primary trapping island, and so on. In complete analogy with the mechanism at η_3^* and η_4^* the stable and unstable manifolds of the period-N fixed points form a homoclinic cycle in the form of a regular polygon, which completely confines the primary trapping island. In the vicinity of the minima the polygons shrink and reexpand. But for $N\geqslant 5$ their areas never shrink to zero resulting in mere minima of $S(\eta)$ instead of zeros. We call this phenomenon *incomplete island collapse*. The reason for incomplete island collapse is well understood and discussed in detail in Sec. II E.

If this picture is correct, we should be able to use the resonance method and find an approximate correlation between the η values where the twist angle of the primary trapping island equals $2\pi/N$, $N=5,6,\ldots$, and the locations of the minima in Fig. 3. Solving the equation $\varphi_N(\eta)=2\pi/N$, $N=5,6,\ldots$, as we did above for $N=3,4$, we obtain the resonance η's η_N^R marked with arrows in Fig. 3(a). As expected, the correlation between the minima and the arrows is best for the deepest minima (closest to complete island collapse) and gets progressively worse for larger η where the minima are far from $S=0$ and then start to vanish altogether. This shows conclusively that, even in the case of incomplete island collapse for $N>4$, near-resonance is the physical reason for the minima in $S(\eta)$ resulting in reduced stability of the trap.

We can even explain the small dips that occur close to the local maxima of $S(\eta)$. The dips are due to higher-order resonances, where the winding number ν is a rational number, i.e., $\nu=M/N$. We checked that the largest dips are due to $\nu=2/(2N+1)$ resonances. In particular we checked that the dip occurring at $\eta\approx 3.95$ [see inset of Fig. 3(a)] is due to a 2/7 resonance, and the dip at $\eta\approx 4.77$ is due to a $\nu=2/9$ resonance.

Using the same general procedure, we now compute analytical approximations to η_3^* and η_4^*. Using the approximate expression (2) for $r_L(t)$ results in

$$\ddot{\xi}(t)-\frac{[2-4\eta\cos(2t)]}{[\eta-\cos(2t)]^2}\xi(t)=0. \tag{11}$$

For large η this is a Mathieu equation [37]. Since we are interested in η values that are larger than 3, but still not

asymptotically large, we start with a Fourier expansion of the drive term in Eq. (11) keeping terms up to order $\cos(2t)$, i.e.,

$$\frac{2-4\eta\cos(2t)}{[\eta-\cos(2t)]^2} = A + B\cos(2t) + \cdots, \tag{12}$$

where

$$A = \frac{1}{\pi}\int_0^{2\pi} \frac{1-2\eta\cos(x)}{[\eta-\cos(x)]^2}dx = -\frac{2\eta}{[\eta^2-1]^{3/2}} \tag{13}$$

and

$$B = \frac{2}{\pi}\int_0^{2\pi} \frac{1-2\eta\cos(x)}{[\eta-\cos(x)]^2}\cos(x)dx$$
$$= -8\{\eta-\sqrt{\eta^2-1}\} - \frac{4}{[\eta^2-1]^{3/2}}. \tag{14}$$

The integrals in Eqs. (13) and (14) were computed using formula 3.6614 of Ref. [38]. Replacing the drive term in Eq. (11) with its expansion (12) results in a Mathieu equation which, in standard form [37], is given by

$$\ddot{\xi}(t) + [a - 2q\cos(2t)]\xi(t) = 0, \tag{15}$$

where $a=-A$ and $q=B/2$. The Mathieu equation (15) has Floquet solutions of the form

$$\xi_F(t) = e^{i\mu t}\Phi(t), \tag{16}$$

where $\Phi(t)$ is π periodic and μ is the characteristic exponent [37]. For small a, as is the case here, we may use formula 20.3.18 of Ref. [37],

$$\cos(\mu\pi) = \left(1 - \frac{a\pi^2}{2} + \frac{a^2\pi^4}{24} + \cdots\right) - \frac{q^2\pi^2}{4}\left[1 + a\left(1-\frac{\pi^2}{6}\right) + \cdots\right] + q^4\left(\frac{\pi^4}{96} - \frac{25\pi^2}{256} + \cdots\right) + \cdots, \tag{17}$$

to connect a and q with μ. For the η_3^* resonance we have $\mu=2/3$ and for the η_4^* resonance we have $\mu=1/2$. Since μ is known and a,q are functions of η only, Eq. (17) can be solved for η to determine η_3^* and η_4^*. However, as it stands, Eq. (17) is too difficult to solve analytically. But expanding Eq. (17) to fourth order in $1/\eta$,

$$\cos(\mu\pi) \approx 1 - \frac{2\pi^2}{\eta^2} + \frac{1}{\eta^4}\left\{\frac{2\pi^4}{3} - \frac{121\pi^2}{16}\right\}, \tag{18}$$

we obtain a quadratic equation in $1/\eta^2$, which can be solved immediately. For $\mu=2/3$ we obtain

$$\eta_3^* = \pi\sqrt{\frac{363-32\pi^2}{66\pi\sqrt{6}-48\pi^2}} = 3.692\,392\,2\ldots \tag{19}$$

and for $\mu=1/2$ we obtain

$$\eta_4^* = \frac{\sqrt{\pi}}{2}\left[\frac{363-32\pi^2}{\sqrt{1089+48\pi^2}-12\pi}\right]^{1/2} = 4.496\,546\,6\ldots. \tag{20}$$

Both values compare favorably with the numerically exact values (10).

E. Connection with bifurcation theory of nonlinear mappings

When they were first discovered about two years ago [19,20] the instabilities of the dynamic Kingdon trap at η_3^* and η_4^* were quite surprising and unexpected, because nearly a decade of research, both theoretical [11,12,14,27,32] and experimental [13,33], did not find so much as a hint of them. In retrospect, however, when the cylindrical dynamic Kingdon trap is put into the general context of nonlinear mappings, the instabilities at η_3^* and η_4^* find a natural explanation.

Let us define the residue R of the linearization Λ [see Eq. (9)] of the mapping M [see Eqs. (3) and (4)] according to [17]

$$R = \tfrac{1}{4}[2 - \mathrm{Tr}\,\Lambda(\eta)] = \sin^2(\pi\nu), \tag{21}$$

where Tr is the trace and ν is the "winding number." The winding number ν and the twist angle φ are connected in the following way:

$$\nu = \frac{\varphi}{2\pi}. \tag{22}$$

Evaluated at the position of the primary fixed point of M, ν counts how many times the primary trapping island rotates around the fixed point during the mapping time π.

The primary fixed point of M is stable for $0<R<1$. It is unstable for $R<0$ or $R>1$. Since R is computed on the basis of the linearization Λ of M, this means that in general linear stability theory is enough for investigating the stability of the primary fixed point of M. However, it is well known [17,18] that linear stability theory may fail for $R=0,1/2,3/4,1$, and *only* for these four exceptional values.

In the case of the dynamic Kingdon trap $R=0$ does not occur for finite η, $R=1/2$ corresponds to the $\nu=1/4$ resonance at $\eta=\eta_4^*$, $R=3/4$ corresponds to the $\nu=1/3$ resonance at $\eta=\eta_3^*$, and $R=1$ corresponds to the first bifurcation at $\eta=\eta_1$.

In the theory of general nonlinear mappings the phase-space scenarios for $R=1/2$ and $R=3/4$ have been studied in detail [17,18]. Indeed, quite generally for nonlinear mappings, in the vicinity of $R=3/4$ the scenario illustrated in Fig. 4, and for $R=1/2$ the scenario illustrated in Fig. 5 unfolds. Thus island collapse is a general, universal phenomenon, not restricted to rf traps. It occurs, e.g., in the annulus billiard [39] and the gravitational wedge billiard [40].

Even the approximately quadratic behavior of $S(\eta)$ in the vicinity of η_3^* and the approximately linear behavior of $S(\eta)$ in the vicinity of η_4^* [see inset of Fig. 3(a)] can be explained. According to Ref. [41] Appendix 7, the unstable period-3 fixed points approach the stable period-1 fixed point with phase-space coordinates proportional to $|\eta-\eta_3^*|$, i.e., the phase-space area of the caging triangle in Fig. 4 is propor-

tional to $(\eta-\eta_3^*)^2$, consistent with the approximately quadratic behavior of $S(\eta)$ close to η_3^* as shown in Fig. 3(a). In the case of the instability at η_4^* the linear dimensions of the caging rectangle are proportional to $|\eta-\eta_4^*|^{1/2}$ [41]. Therefore the phase-space area of the caging rectangle behaves like $|\eta-\eta_4^*|$ in the vicinity of η_4^*, consistent with the linear behavior of $S(\eta)$ close to η_4^* [see Fig. 3(a)].

An important remark is now in order. Although all rf traps correspond to some nonlinear mapping M, it is not guaranteed that M (i) has a (stable) period-1 fixed point at all and (ii) that $R=1/2$ or $R=3/4$, leading to trap instabilities, exist at all. Indeed plenty of mappings are known [42] which do not have stable period-1 fixed points, and in which scenarios akin to those displayed in Figs. 4 and 5 do not exist. Therefore the existence of $R=1/2$ and $R=3/4$ instabilities cannot be guaranteed *a priori*, just because traps correspond to nonlinear mappings. In other words, if some rf trap T exhibits $R=1/2$ and/or $R=3/4$ instabilities, this is a nontrivial property of T. Therefore, the purpose of the remainder of this paper is to show that additional rf traps exist which exhibit $R=1/2$ and $R=3/4$ instabilities.

III. KICKED KINGDON TRAP

In this section we study the kicked Kingdon trap. It is obtained by replacing the smooth drive in the force term of Eq. (1) with a series of δ function kicks according to

$$-1+2\eta\cos(2t)\sim\frac{\alpha}{2}\delta_\pi(t)-\beta\delta_\pi\left(t-\frac{\pi}{2}\right)+\frac{\alpha}{2}\delta_\pi(t-\pi), \tag{23}$$

where α and β are given by

$$\alpha=\frac{\pi}{2}(\eta-1),\quad \beta=\frac{\pi}{2}(\eta+1), \tag{24}$$

and

$$\delta_\pi(t)=\sum_{m=-\infty}^{\infty}\delta(t-m\pi)=\frac{1}{\pi}\sum_{m=-\infty}^{\infty}e^{2imt} \tag{25}$$

is the π-periodic δ function. For the choice (24) the left- and right-hand sides of Eq. (25) are identical up to terms $\cos(2t)$. Although Eq. (23) could equally well be written as $\alpha\delta_\pi(t)-\beta\delta_\pi(t-\pi/2)$, we chose the particular form (23) since it indicates more clearly the proper construction of the one-cycle kick map, which starts with a kick of strength $\alpha/2$ followed by free motion of duration $\Delta t=\pi/2$, followed by a kick of strength $-\beta$, subsequent free motion of duration $\Delta t=\pi/2$, and completed with a kick of strength $\alpha/2$. The mapping thus constructed is different from the mapping studied in Ref. [14]. The choice (23) makes the resulting one-cycle kick map more symmetric and places the center of the primary trapping island at $p=0$, where it occurs for the continuously driven (cw-driven) trap.

The one-cycle mapping defined by Eq. (23) takes the phase-space point (r,p) at $t=0$ to (r',p') at $t=\pi$. It is given explicitly by

$$r'=r+\pi p+\frac{\pi\alpha}{2r}-\frac{\pi\beta}{2r+\pi p+\frac{\pi\alpha}{2r}},$$

$$p'=p+\frac{\alpha}{2r}-\frac{2\beta}{2r+\pi p+\frac{\pi\alpha}{2r}}+\frac{\alpha}{2r+2\pi p+\frac{\pi\alpha}{r}-\frac{2\pi\beta}{2r+\pi p+\frac{\pi\alpha}{2r}}}. \tag{26}$$

The first-order fixed point $(r_f^{(k)},p_f^{(k)})$ of the kick map (26), the center of the primary trapping island, is located at

$$r_f^{(\mathrm{k})}=\frac{\pi}{4}(\eta-1)=\frac{\alpha}{2},\quad p_f^{(\mathrm{k})}=0. \tag{27}$$

This can be compared with the location $(r_f^{(\mathrm{cw})},p_f^{(\mathrm{cw})})$ of the fixed point of the cw-driven trap. According to Eq. (2) we have

$$r_f^{(\mathrm{cw})}\approx\frac{1}{\sqrt{2}}(\eta-1),\quad p_f^{(\mathrm{cw})}=0. \tag{28}$$

The relative error between the two is constant in η and given by

$$\left|\frac{r_f^{(\mathrm{k})}-r_f^{(\mathrm{cw})}}{r_f^{(\mathrm{cw})}}\right|=\frac{\pi\sqrt{2}}{4}-1, \tag{29}$$

which amounts to about 11%. This is a good accuracy given the simple kick approximation (23).

The phase-space dynamics of Eq. (1) and the kick map (26) are qualitatively the same. We illustrate this in Fig. 3(b), which shows the trapping efficiency $S(\eta)$ for the kick map (26) computed in the same way as for the cw-driven trap. Comparing Figs. 3(a) and 3(b), we see that $S(\eta)$ is indeed qualitatively the same. In particular $S(\eta)$ of the kick map also has two zeros close to η_3^* and η_4^*. We call them η_3^*(kick) and η_4^*(kick), respectively.

In the case of the kick map we can prove analytically that the mechanism responsible for the instabilities at η_3^*(kick) and η_4^*(kick) is in fact due to a collision between the center of the primary trapping island and a degenerate set of unstable period-3 and period-4 fixed points, respectively. Focussing on the case η_3^*(kick), we compute the third-order fixed point of Eq. (26) by starting at $(r,0)$ and iterating (26) three times. The condition to return to $(r,0)$ after three iterations leads to the equation

$$F(r)=[x(r)-r]\left[\frac{2}{\pi}-\frac{\alpha}{2rx(r)}\right]+\left[\frac{x(r)}{\pi}+\frac{\alpha}{2x(r)}\right]-\sqrt{\frac{x^2(r)}{\pi^2}+1+\frac{\alpha}{\pi}}=0, \tag{30}$$

where

$$x(r) = r + \frac{\pi\alpha}{2r} - \frac{2\pi\beta r}{4r^2 + \pi\alpha}. \tag{31}$$

For η close to $\eta_3^*(\text{kick})$ $F(r)$ is locally quadratic. One of its zeros corresponds to the period-1 fixed point at $r=\alpha/2$, the other to the period-3 fixed point. A collision of the two fixed points occurs if the zero at $r=\alpha/2$ becomes degenerate, i.e., $F'(\alpha/2)=0$. When this happens, it also determines the exact value of $\eta_3^*(\text{kick})$. The condition $F'(\alpha/2)=0$ yields

$$1 - \frac{12\pi^2}{\alpha\beta} - \frac{2\pi}{\alpha} + \frac{16\pi^3}{\alpha^2\beta} + \frac{4\pi^2 - \alpha\beta}{(\alpha + 2\pi)\beta} = 0. \tag{32}$$

This equation can be solved for η and yields

$$\eta_3^*(\text{kick}) = \tfrac{1}{3}\sqrt{105} = 3.415\,650\,2\ldots. \tag{33}$$

The existence of this solution proves that the degeneracy actually happens. Its numerical value is close to η_3^* of the cw-driven trap [see Eq. (10)].

In complete analogy to the computation of $\eta_3^*(\text{kick})$ we compute $\eta_4^*(\text{kick})$. We obtain

$$\eta_4^*(\text{kick}) = \sqrt{17} = 4.123\,105\,6\ldots. \tag{34}$$

The existence of this solution proves that indeed a set of degenerate period-4 fixed points collides with the period-1 center of the trapping island at $\eta_4^*(\text{kick})$ of the kick map. The numerical value of $\eta_4^*(\text{kick})$ is close to η_4^* of the cw-driven trap [see Eq. (10)].

The kicked Kingdon trap offers the possibility of checking analytically that the "resonance method" yields the same result as the computation of $\eta_3^*(\text{kick})$ and $\eta_4^*(\text{kick})$ via direct fixed point calculations as done above. In order to use the resonance method, we linearize Eq. (26) obtaining the phase-space mapping

$$\begin{pmatrix} r' \\ p' \end{pmatrix} = \tilde{\Lambda}(\eta) \begin{pmatrix} r \\ p \end{pmatrix}, \tag{35}$$

where

$$\tilde{\Lambda}_{11} = \frac{\partial r'}{\partial r} = 1 - \frac{\pi\alpha}{2r^2} - \frac{2\pi\beta(\pi\alpha - 4r^2)}{[4r^2 + 2\pi pr + \pi\alpha]^2},$$

$$\tilde{\Lambda}_{12} = \frac{\partial r'}{\partial p} = \pi + \frac{4\pi^2\beta r^2}{[4r^2 + 2\pi pr + \pi\alpha]^2},$$

$$\tilde{\Lambda}_{21} = \frac{\partial p'}{\partial r} = \frac{\alpha}{2r^2} - \frac{2}{\pi} + \left[\frac{2}{\pi} - \frac{\alpha}{2(r')^2}\right]\frac{\partial r'}{\partial r},$$

$$\tilde{\Lambda}_{22} = \frac{\partial p'}{\partial p} = -1 + \left[\frac{2}{\pi} - \frac{\alpha}{2(r')^2}\right]\frac{\partial r'}{\partial p}. \tag{36}$$

Since $\tilde{\Lambda}$ is an area-preserving mapping, its determinant is 1. Its residue, evaluated at $r=r'=\alpha/2$, $p=0$, is

$$R(\eta) = \frac{8}{\eta^2 - 1}. \tag{37}$$

Since $R[\eta_3^*(\text{kick})]=3/4$ (see Sec. II E), it can be checked immediately that $\eta_3^*(\text{kick})=\sqrt{105}/3$, and since $R[\eta_4^*(\text{kick})]=1/2$, $\eta_4^*(\text{kick})=\sqrt{17}$. This confirms Eqs. (33) and (34) together with the equivalence of the resonance method and the fixed point collision method.

In the case of the kicked trap the resonances $\eta_N^R(\text{kick})$ for $N\geqslant 5$ are obtained analytically by solving Eq. (21) for $\nu=1/N$, $N\geqslant 5$ with R given by Eq. (37). This leads to the equation

$$\eta_N^R = \left[1 + \frac{16}{1 - \cos(2\pi/N)}\right]^{1/2}. \tag{38}$$

Explicitly, $\eta_5^R=4.914\,8\ldots$, $\eta_6^R=\sqrt{33}$, $\eta_7^R=6.595\,1\ldots$, $\eta_8^R=(33+16\sqrt{2})^{1/2}$, $\eta_9^R=8.330\,0\ldots$. These values are marked by the arrows in Fig. 3(b). Again we see that the correlation between the minima and the arrows is best for the deepest minima, in particular for the first minimum at η_5^R, where $S(\eta)$ nearly reaches $S=0$.

IV. SPHERICAL DYNAMIC KINGDON TRAP

An important question is whether the instabilities at η_3^* and η_4^* in the cylindrical dynamic Kingdon trap are accidents, or whether this result is structurally stable. As discussed at the end of Sec. II E this is a nontrivial question, and it is far from guaranteed that other traps with these properties exist. Thus the purpose of this section is to prove that in fact another trap exists, the spherical dynamic Kingdon trap, which shows instabilities in analogy to the instabilities occurring at η_3^* and η_4^* in the cylindrical dynamic Kingdon trap.

Figure 6 shows a sketch of the spherical dynamic Kingdon trap. It consists of two nested ideally conducting shells (a spherical capacitor) with a superposition of ac and dc voltages applied between them. The dimensionless equation of motion of the spherical dynamic Kingdon trap is given by [14]

$$\frac{d^2r}{dt^2} = -[1 - 2\eta\cos(2t)]\frac{1}{r^2}. \tag{39}$$

Although this type of trap was studied intensively both theoretically [14] and experimentally [13], instabilities were not previously reported to occur in this type of trap. Figures 7 and 8, however, show that the $N=3$ and $N=4$ resonances produce the same type of instabilities in the spherical dynamic Kingdon trap as already seen in the cylindrical dynamic Kingdon trap (see Sec. II and Figs. 4 and 5). The exact locations of the $N=3$ and $N=4$ collapse points were determined using the same methodology as was used in the case of the cylindrical dynamic Kingdon trap (see Sec. II D). As a result we obtain that the primary trapping island of the spherical dynamic Kingdon trap vanishes at $\eta_3^*=3.161\,713\,2\ldots$ and $\eta_4^*=3.864\,074\,7\ldots$.

Figures 7(a)–7(c) and 8(a)–8(c) show the collapse scenarios for the $N=3$ and $N=4$ resonances. They are very simi-

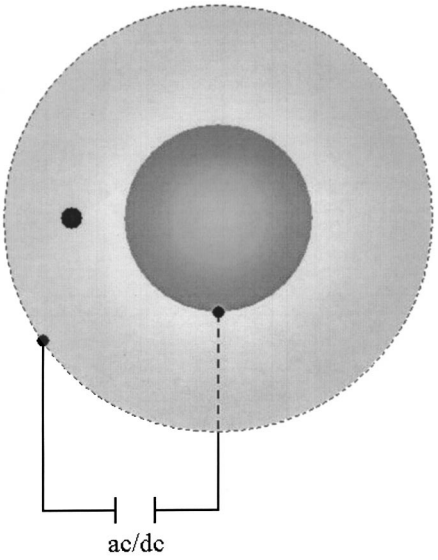

FIG. 6. Sketch of the spherical dynamic Kingdon trap. A superposition of ac and dc voltages is applied between two concentric ideally conducting shells. The resulting oscillating electric field produces dynamical trapping of a charged particle in the free space between the two shells.

lar to the corresponding scenarios exhibited by the cylindrical dynamic Kingdon trap [compare Figs. 4(a)–4(c) and 5(a)–5(c)]. In particular even the orientations of the primary trapping islands before and after the fixed point collisions are the same. Thus the instabilities exhibited by the cylindrical dynamic Kingdon trap are not an isolated phenomenon, but they are shared by at least one other trap: the spherical dynamic Kingdon trap. In the following section we show that even the Paul trap, the most important and most widely used rf trap, exhibits the $N=3$ and $N=4$ instabilities.

V. PAUL TRAP

Figure 9 shows a sketch of the Paul trap. It consists of an ideally conducting hyperbolic ring electrode and two ideally conducting hyperbolic end caps [1–3]. Since its invention by Paul and collaborators in the 1950s the Paul trap has evolved into one of the most important tools of modern atomic physics. The dimensionless equations of motion for a single charged particle stored in a Paul trap are given by

$$\frac{d^2}{dt^2}\begin{pmatrix} X \\ Y \\ Z \end{pmatrix} = -\left[a - 2q\cos(2t)\right]\begin{pmatrix} X \\ Y \\ -2Z \end{pmatrix}, \tag{40}$$

where a and q, proportional to the applied dc and ac voltages, respectively, are the two dimensionless control parameters of the trap and X,Y,Z are the particle's coordinates. The Paul trap is globally stable [i.e., the solutions of Eq. (40) are bounded], if the trap is operated with parameter combinations (q,a) chosen from the interior of the stability area defined by the lines c,d,e,f in Fig. 10. In this respect the Paul trap is completely different from the dynamic Kingdon traps where, in addition to the control parameter setting, the stability of a trapped particle also depends on the initial conditions of its associated phase-space trajectory.

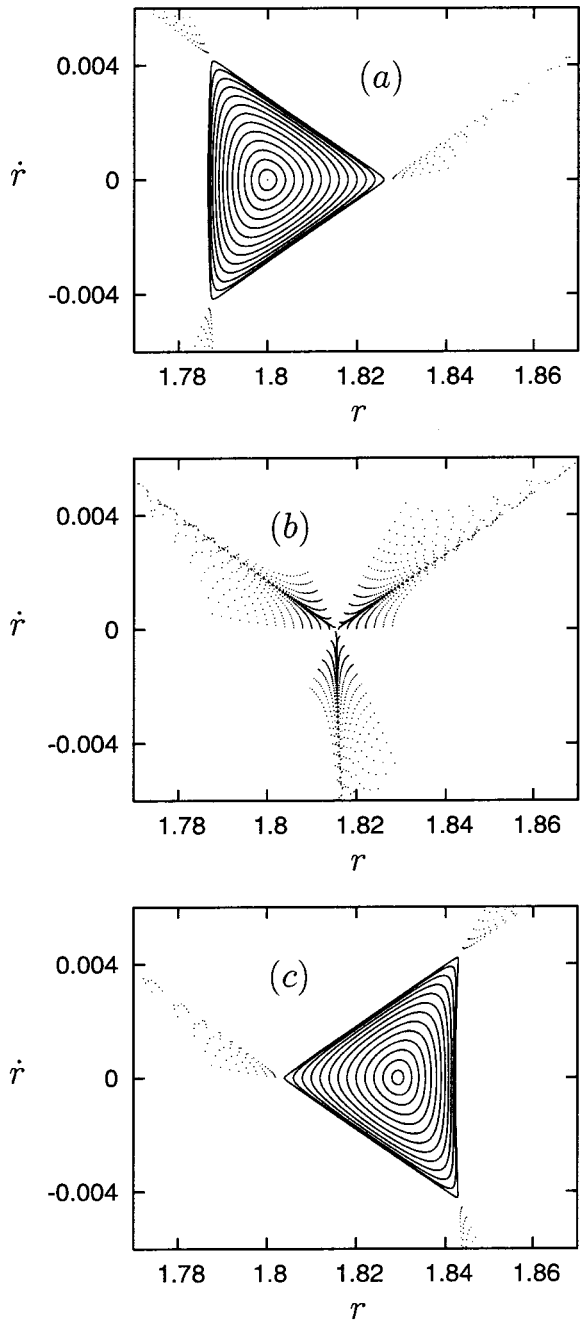

FIG. 7. Island collapse for the spherical dynamic Kingdon trap at the $N=3$ resonance. (a) $\eta=3.13$ (immediately before the collapse point), (b) $\eta=\eta_3^*=3.161\,713\,2\ldots$ (at the collapse point), (c) $\eta=3.19$ (immediately after the collapse point). The scenario is reminiscent of the scenario exhibited by the cylindrical dynamic Kingdon trap at the $N=3$ resonance shown in Fig. 4(a)–4(c).

With the help of Mathieu functions [37] the linear, single-particle equations (40) are integrable and instabilities due to nonlinear resonance scenarios do not occur. This changes drastically if two or more particles are simultaneously stored in the trap. In this section we study the two-particle case in detail.

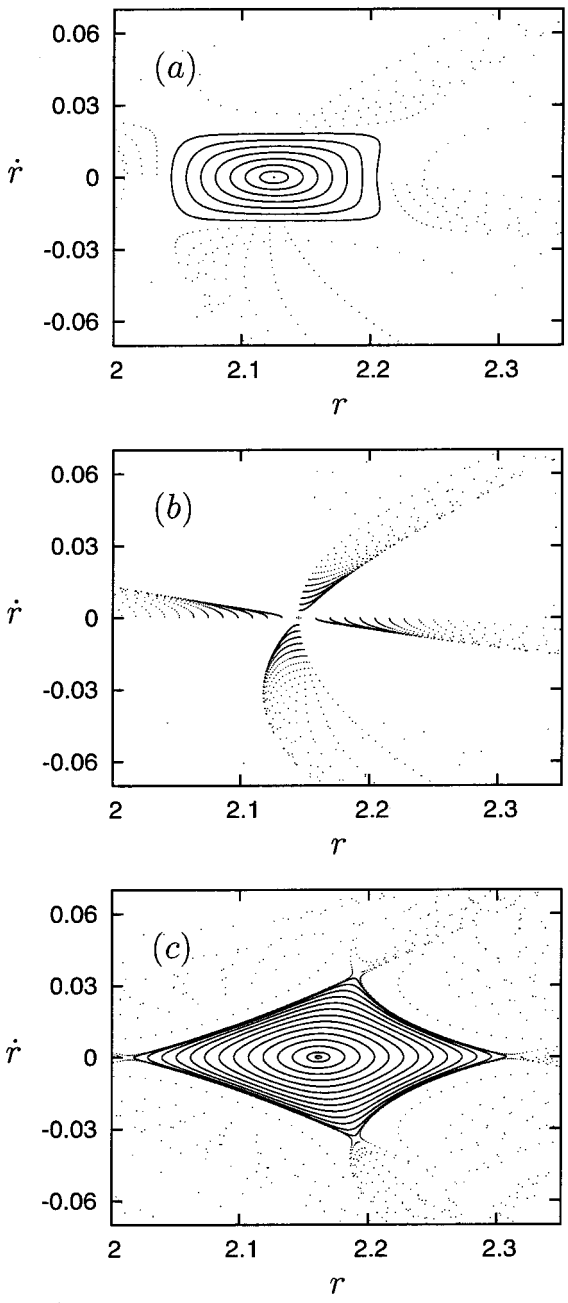

FIG. 8. Island collapse for the spherical dynamic Kingdon trap at the $N=4$ resonance. (a) $\eta=3.82$ (immediately before the collapse point), (b) $\eta=\eta_4^*=3.864\,074\,7\ldots$ (at the collapse point), (c) $\eta=3.9$ (immediately after the collapse point). The scenario is reminiscent of the scenario exhibited by the cylindrical dynamic Kingdon trap at the $N=4$ resonance shown in Fig. 5(a)–5(c).

The center of mass $\vec{X}=(X,Y,Z)=(\vec{X}_1+\vec{X}_2)/2$ of two simultaneously stored particles with coordinates $\vec{X}_1=(X_1,Y_1,Z_1)$ and $\vec{X}_2=(X_2,Y_2,Z_2)$ satisfies the linear equations of motion (40) and is uninteresting in the present context. The relative coordinate $\vec{x}=(x,y,z)=\vec{X}_1-\vec{X}_2$ satisfies the equations of motion

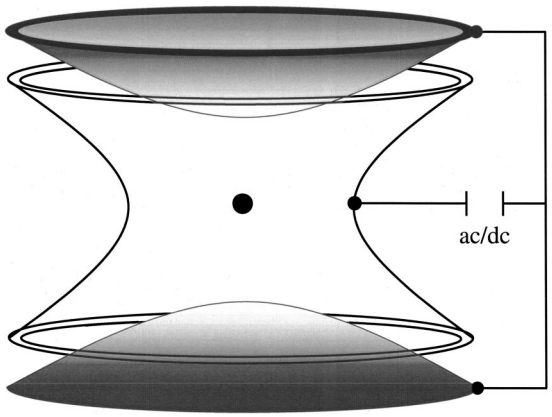

FIG. 9. Sketch of the Paul trap. A superposition of ac and dc voltages is applied between an ideally conducting hyperbolic ring electrode and two ideally conducting hyperbolic end caps.

$$\frac{d^2}{dt^2}\begin{pmatrix}x\\y\\z\end{pmatrix}=-[a-2q\cos(2t)]\begin{pmatrix}x\\y\\-2z\end{pmatrix}+\frac{\vec{x}}{|\vec{x}|^3}. \qquad (41)$$

This equation is nonlinear and its associated stroboscopic mapping, i.e., the mapping that takes $\vec{x}(n\pi)$ to $\vec{x}[(n+1)\pi]$, may therefore exhibit $N=3$ and $N=4$ instabilities as discussed in Sec. II E. This is indeed the case. But before we are ready to investigate the $N=3$ and $N=4$ instabilities of the

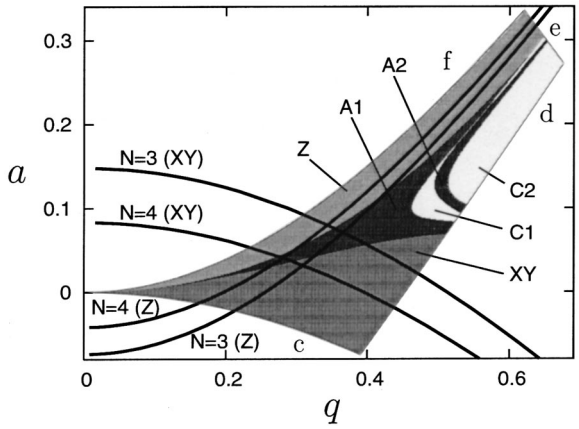

FIG. 10. Stability diagram of the Paul trap. The trap is globally stable if operated with a (q,a) control parameter setting taken from inside of the stability region framed by the curves c,d,e, and f. The different shades of gray indicate control parameter combinations (q,a) where two simultaneously stored ions in their lowest-energy state are z aligned (light shade of gray, labeled "Z"), xy-aligned (darker shade of gray, labeled "XY"), and aligned at an angle with respect to the z axis (dark shade of gray, labeled "A_1" and "A_2"). The areas A_1 and A_2 are not contiguous. Areas C_1 and C_2 separated by area A_2 are chaotic regions. The heavy lines labeled $N=3(XY)$ and $N=4(XY)$ correspond to (q,a) parameter combinations where a two-ion crystal in the xy plane experiences an $N=3$ ($N=3$) resonance and breaks up. The heavy lines labeled $N=3(Z)$ and $N=4(Z)$ correspond to (q,a) parameter combinations where a two-ion crystal aligned with the z axis experiences an $N=3$ ($N=4$) resonance and breaks up.

Paul trap in detail we have to discuss the possible two-ion configurations in a Paul trap.

Stationary minimal-energy configurations in the Paul trap are known as two-ion crystals [43]. It is well known [43,44] that there are three possibilities for the alignment of two-ion crystals in the Paul trap. The two ions of the crystal can either align with the z axis, lie in the xy plane, or form an angle with the z axis. Which of the three stationary configurations is actually selected depends on the parameter combination (q,a) with which the trap is operated. Two ions in their lowest-energy configuration are aligned with the z axis if (q,a) is selected from the lightly shaded region of the stability diagram shown in Fig. 10 (labeled "Z"). The two ions will lie in the xy plane if (q,a) is selected from the darker area of the stability diagram in Fig. 10 (labeled "XY") and the two ions will form an angle with the z axis if (q,a) is selected from the two areas with the darkest shade of gray in Fig. 10 (labeled "A_1" and "A_2"). The white areas of the stability diagram in Fig. 10, labeled "C_1" and "C_2," correspond to chaotic regions where simple stationary ion configurations are hard to find.

We start with discussing z-aligned ion crystals. In this case $x=y=0$ for all time and only the z equation of Eq. (41) needs to be considered. Using the methodology discussed in Sec. II D we determined the locations of the $N=3$ and $N=4$ resonances of z-aligned ion crystals. Since the Paul trap depends on two control parameters, the $N=3$ and $N=4$ instabilities are located on lines in the stability diagram of Fig. 10 labeled $N=3(Z)$ and $N=4(Z)$, respectively. Since the z equation of Eq. (41) is defined for the entire range of q values shown in Fig. 10, we plotted the two curves $N=3(Z)$ and $N=4(Z)$ in the entire interval $0<q\sim 0.7$. In complete analogy to the z-aligned case we also plotted the lines $N=3(XY)$ and $N=4(XY)$, which correspond to xy-aligned ion crystals.

Figure 11 shows that on the curve $N=3(XY)$ the primary trapping island vanishes just like it did in the analogous cases of the cylindrical and the spherical dynamic Kingdon traps. But Fig. 11(b) shows that although the primary trapping island is destroyed for (q,a) on $N=3(XY)$, there is a fundamental difference compared with the dynamic Kingdon traps: even at the $N=3$ resonance point large, stable, secondary, third-order islands remain. Figure 12 shows the island destruction scenario for the case $N=4$. Here, too, the primary island vanishes, but a chain of large, stable, secondary, fourth-order islands remains.

We now demonstrate that our prediction of the occurrence of $N=3$ and $N=4$ instabilities in the Paul trap can be tested experimentally. We focus on the $N=3$ instability at $(q=0.5712, a=0.25)$. A phase-space portrait of this case is shown in Fig. 13(a). The primary trapping island is clearly destroyed. Figure 13(b) is a composite phase-space portrait in analogy to Fig. 2. Figure 13(b) shows the primary trapping island at $q=q_1=0.56$. For increasing q the primary trapping island moves to the left, where we show it again at $q=q_2=0.59$. The critical point, at $q=q^*=0.5712$, as shown in Fig. 13(a), is located in between the two trapping islands.

In order to reveal the $N=3$ resonance at $q=q^*$, we ran the following simulation. We started a z-aligned two-ion crystal close to the center of the trapping island at $q=q_1$. We then increased the control parameter q at a rate of $\dot{q}=4\times 10^{-9}$ per cycle. This way the two-ion crystal is "dragged" [45] very slowly (adiabatically) towards the instability at $q=q^*$, which is reached after about 2.8×10^6 cycles. If we assume that the trap is operated at 11 MHz [46], this corresponds to about 0.25 s real time. Once the instability is reached, the two-ion crystal quickly breaks up (on the scale of about 200 cycles, or about 18 μs) and forms a cloud state [46]. In the cloud state the two ions are no longer locked into a regular, crys-

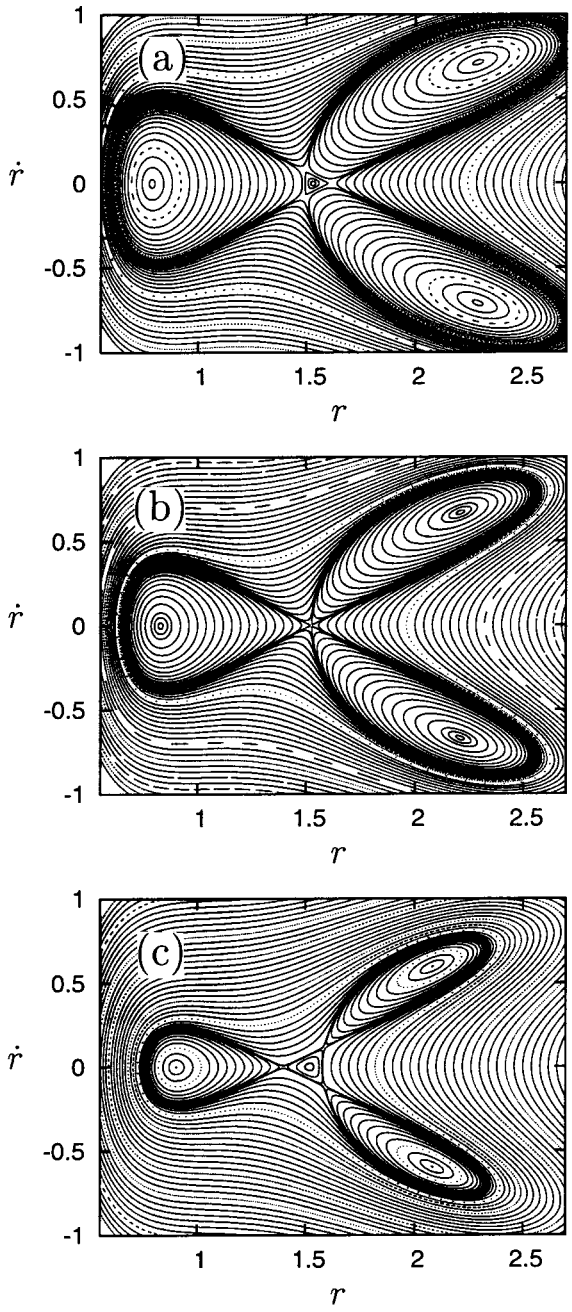

FIG. 11. Paul trap $N=3$ resonance scenario. $a=0.05$, and (a) $q=0.412$, (b) $q=0.4137\approx q^*$, and (c) $q=0.416$. In analogy to Figs. 4(a)–4(c) the primary trapping island vanishes at q^*. In contrast to Figs. 4(a)–4(c) the three large, stable elliptic islands stay intact before, during, and after the instability.

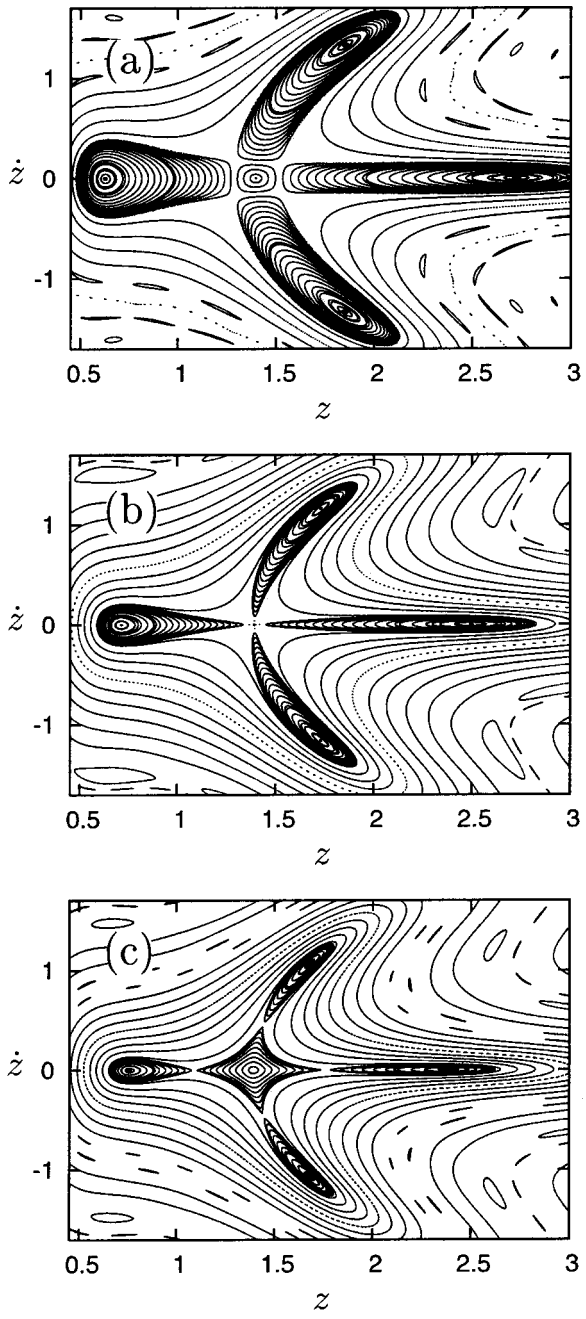

FIG. 12. Paul trap $N=4$ resonance scenario. $a=0.3$, and (a) $q=0.6055$, (b) $q=0.605\,654\approx q^*$, and (c) $q=0.6057$. In analogy to Figs. 5(a)–5(c) the primary trapping island vanishes at q^*. In contrast to Figs. 5(a)–5(c) the four large, stable, elliptic islands stay intact before, during, and after the instability.

talline configuration, but move quasi-independently on chaotic trajectories [47]. As shown in Fig. 13(b), the crystal breaks up along the unstable manifolds of the critical point at $q=q^*$. Since it has already been demonstrated experimentally that it is possible to tell crystals from clouds [46], our simulation shows convincingly that the existence of $N=3$ instability points can be tested experimentally.

We also ran simulations concerning the $N=4$ instabilities. These simulations show that crystals dragged towards the

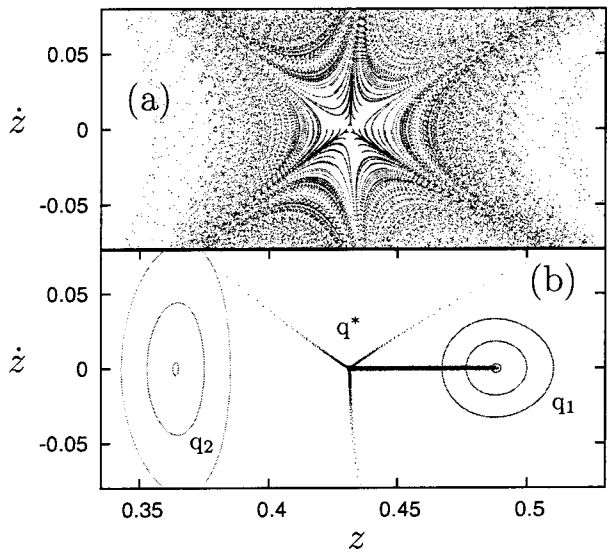

FIG. 13. Destruction of a two-ion crystal at the Paul trap $N=3$ instability at $a=0.25$, $q=0.5712\approx q^*$. (a) Phase-space portrait for $a=0.25$, $q=0.5712$ illustrating the destruction of the primary trapping island. (b) Composite phase-space portrait showing the primary trapping island at $a=0.25$, $q=q_1=0.56$ and $a=0.25$, $q=q_2=0.59$. Also shown is the phase-space trajectory of a z-aligned two-ion crystal dragged slowly from q_1 to q^*, breaking up at q^* along the unstable manifolds of the fixed point at q^* [see panel (a)] and thus revealing the presence of the $N=3$ instability at q^*.

$N=4$ resonance lines also break up. Thus the $N=4$ instabilities are also accessible to experimental testing.

VI. DISCUSSION

The Kingdon equations (1) and (39) are special cases of the generalized Mathieu equation [11]

$$\frac{d^2r}{dt^2}+[1-2\eta\cos(2t)]r^{\gamma}=0, \tag{42}$$

which describes a whole range of charged-particle rf traps. For $\gamma=1$, e.g., we obtain the equation of motion (40) of the single-particle Paul trap, $\gamma=-1$ corresponds to the cylindrical dynamic Kingdon trap (Sec. II), and $\gamma=-2$ corresponds to the spherical dynamic Kingdon trap (Sec. IV). The case $\gamma=1$ is not interesting, since it corresponds to the linear Mathieu equation [37]. Since we found $N=3$ and $N=4$ instabilities for both the cylindrical (Sec. II) and the spherical (Sec. IV) dynamic Kingdon traps, it is possible, though not guaranteed (see remark at the end of Sec. II E) that island collapse is a generic property of the generalized Mathieu equation (42).

The instabilities of the cylindrical dynamic Kingdon trap at η_3^* and η_4^* manifest themselves most clearly in the stability function $S(\eta)$ discussed in Sec. II. Although $S(\eta)$ clearly makes the case for instability at η_3^* and η_4^*, the curve itself has to be taken with a grain of salt. First of all it is well known [48,49] that in general the borders of stability islands are fractal. Although the phase-space resolution chosen to produce Fig. 3 is high [it took about one month of CPU time

on a six-processor cluster computer to produce $S(\eta)$ shown in Fig. 3(a)], the phase-space resolution is definitely not fine enough to even begin to resolve the fractal borders of the stable islands. Still, the fractal nature of the borders results in some "roughness" of $S(\eta)$, which is visible in Fig. 3 from about $\eta=6$ on. For the purposes of this paper, however, an ultra-accurate $S(\eta)$ is not necessary. For our purposes it is enough to know the approximate behavior of $S(\eta)$ with a moderate resolution (for instance as chosen to produce Fig. 3), since $S(\eta)$'s purpose was more than adequately accomplished when it alerted us to the possible existence of η_3^* and η_4^*. The subsequent investigation of the instability of the trap at η_3^* and η_4^* in Sec. II does not at all rely on $S(\eta)$, but does instead rely exclusively on visual inspection of detailed Poincaré sections, analytical arguments, and numerical computations of resonance values.

We stopped our systematic survey of $S(\eta)$ at $\eta=10$. This raises the question of whether there may be further instabilities for $\eta>10$. We think that this is unlikely because of the following four reasons. (i) As mentioned in Sec. II E, linear stability theory breaks down *only* for the four special values $R=0,1/2,3/4,1$. In the case of the kicked Kingdon trap, we have $0<R<8/99$ [see Eq. (21)] for $\eta>10$, which implies two things: (a) $0<R<8/99$ does not include any of the exceptional R values and (b) $0<R<8/99$ is a subinterval of $0<R<1$ for which the primary trapping island is stable (see Sec. II E). Thus the kicked Kingdon trap is stable for $\eta>10$. (ii) Since we showed in Sec. III that the kicked Kingdon trap is an excellent model for the cw-driven Kingdon trap, and since the trapping efficiencies $S(\eta)$ are qualitatively similar for the two traps [see Fig. 3(a) and 3(b)], we conclude that since the kicked Kingdon trap is stable for $\eta>10$ [see (i) above], so is the cw-driven trap. (iii) Expanding Eqs. (13) and (14) to fourth order in $1/\eta$ it can be shown that Eq. (15) is stable for $\eta>10$. (iv) The larger η, the more accurate the pseudopotential approximation [11,12,35]. This is so, because one of the conditions of the applicability of the pseudopotential approximation is that the amplitude of the micromotion is small compared with the "guiding-center" or "macromotion" [35,50]. In our case the guiding center is the geometric center of the limit cycle $[r_L(t),\dot{r}_L(t)]$, which is stationary for fixed η. According to Eq. (A2) the geometric center of the limit cycle is located approximately at $\eta/\sqrt{2}$ and the amplitude of the micromotion, again according to Eq. (A2), is approximately $1/\sqrt{2}$. Therefore,

$$\frac{\text{amplitude of micromotion}}{\text{amplitude of macromotion}} \approx \frac{1}{\eta} \to 0 \quad \text{for } \eta \to \infty. \tag{43}$$

Therefore we trust the stability prediction of pseudopotential theory for $\eta>10$.

Some preliminary surveys of the phase space of the kicked and the cw-driven cylindrical dynamic Kingdon traps indicate that both traps are completely unstable at η_3^*, i.e., at $\eta=\eta_3^*$ their phase space does not seem to exhibit any stable islands whatsoever. A system without any stable islands is a hyperbolic dynamical system if certain additional conditions are met [28,34]. Only very few hyperbolic systems are known, and even fewer model real physical systems. We know of only one such system, where the absence of stable islands was proved analytically: the kicked one-dimensional hydrogen atom [51,52]. The dynamic Kingdon traps at η_3^* may be additional candidates. Numerical evidence, however, is not proof. If the absence of islands at η_3^* is indeed confirmed, a proof may be provided using the methods in Refs. [51,52].

Compared with the Paul trap the instabilities of the dynamic Kingdon traps are particularly devastating. In the Paul trap encountering an $N=3$ or an $N=4$ instability merely means the breakup of an ordered ion configuration; the ions themselves remain trapped. In the dynamic Kingdon traps, however, encountering an $N=3$ or an $N=4$ instability means the complete loss of the particle from the trap.

As shown by the insets of Fig. 3 the shrinking and reexpansion of the primary trapping island of the cylindrical dynamic Kingdon trap takes place in a narrow η interval of $\Delta\eta\approx 0.1$. In order to resolve it, an η resolution of $\delta\eta=0.01$, as chosen in our calculations, may be desirable. The question arises whether a resolution of $\delta\eta=0.01$ can be realized experimentally. Using the relation [12]

$$\eta = \frac{V_{\text{ac}}}{2V_{\text{dc}}}, \tag{44}$$

where V_{ac} and V_{dc} are, respectively, the ac and dc voltages applied to the trap, the necessary η resolution translates into voltage resolutions. In order to answer the question of whether $\delta\eta=0.01$ can be implemented experimentally, we use the example of a possible experimental setup for trapping Mg^+ ions as discussed in Ref. [12]. In this example it is assumed that the trap is operated with a dc voltage of $V_{\text{dc}}=100$ V. At η_3^*, according to Eq. (44), this translates into $V_{\text{ac}}=723$ V. Keeping V_{dc} fixed, $\delta\eta=0.01$ translates into $\delta V_{\text{ac}}=2$ V. Changing a voltage of about 700 V in steps of 2 V is certainly technically feasible. It seems to us that even finer resolutions should be technically possible, which would allow an experimental test of the existence and locations of the instability points in the cylindrical dynamic Kingdon trap.

VII. SUMMARY AND CONCLUSIONS

In this paper we investigated in detail recently discovered instabilities in several types of rf traps including the Paul trap, the most widely used and most important rf trap. We showed that the instabilities are due to island collapse, i.e., the vanishing of the primary trapping island due to a collision of the center period-1 fixed point of the primary trapping island with a set of collapsed, unstable period-3 and a set of collapsed, unstable period-4 fixed points, respectively. We computed accurate values of the critical control parameters for four different types of rf traps, the cw-driven cylindrical and spherical dynamic Kingdon traps, the kicked cylindrical Kingdon trap and the Paul trap. For the cw-driven cylindrical dynamic Kingdon trap we computed analytical approximations to η_3^* and η_4^* which are in good agreement with the exact values of the critical control parameters in this

case. In the case of the kicked trap we were able to compute exact analytical expressions for the critical control parameters where the instabilities occur. We also observed and explained reduced stability of the kicked and cw-driven cylindrical dynamic Kingdon traps at additional values η_N^R, $N \geqslant 5$ of the traps' control parameter η. For experimentalists knowledge of the exact positions of the dynamic instabilities of rf traps is essential for successfully operating these traps in the laboratory. For theorists the existence of the dynamic instabilities in rf traps opens up plenty of possibilities for further research into the nonlinear properties of these traps. A case in point is our preliminary numerical result on the absence of stable islands in the dynamic Kingdon traps at $\eta = \eta_3^*$, which, if confirmed, provides the opportunity of adding another member to the very small set of experimentally relevant completely chaotic, hyperbolic systems.

ACKNOWLEDGMENTS

The authors gratefully acknowledge financial support by the National Science Foundation, Grant No. PHY-9984075.

APPENDIX: LIMIT CYCLE

Since the limit cycle $r_L(t)$ of the cylindrical dynamic Kingdon trap is so important for organizing the phase-space dynamics of this trap, we present here a high-accuracy analytical approximation of $r_L(t)$. As shown in Fig. 2 the limit cycle determines the fixed point of the primary trapping island. Therefore the calculations presented here are also of direct relevance for a high-accuracy analytical calculation of the position of the center of the primary trapping island.

Since $r_L(t)$ is π-periodic, and since Eq. (1) is symmetric under $t \to -t$, we expand it into a Fourier-cos series

$$r_L(t) = \sum_{m=0}^{\infty} A_m \cos(2mt). \tag{A1}$$

Keeping only the first two terms in Eq. (A1) defines the truncated approximation $r_L^{(2)}(t)$. Inserting $r_L^{(2)}(t)$ into Eq. (1), comparing terms, and selecting the solution with $r_L^{(2)}(t) > 0$ for all t, we obtain

$$r_L^{(2)}(t) = \frac{\eta}{\sqrt{2}} - \frac{1}{\sqrt{2}} \cos(2t). \tag{A2}$$

This solution was already computed in Ref. [11] and was studied in the presence of damping in Ref. [32]. It is also the basis for computing the analytical approximations to η_3^* and η_4^* in Sec. II D. For $\eta = 5$ the approximate limit cycle $r_L^{(2)}(t)$ is shown in Fig. 14 (long dashes). Although only two terms were kept in Eq. (A1), $r_L^{(2)}(t)$ is surprisingly close to the exact limit cycle (full line in Fig. 14).

A high-accuracy approximation of $r_L(t)$ is obtained by keeping the first three terms in Eq. (A1). Inserting

$$r_L^{(3)}(t) = A_0 + A_1 \cos(2t) + A_2 \cos(4t) \tag{A3}$$

into Eq. (1), we obtain the following nonlinear algebraic system of equations for the expansion coefficients:

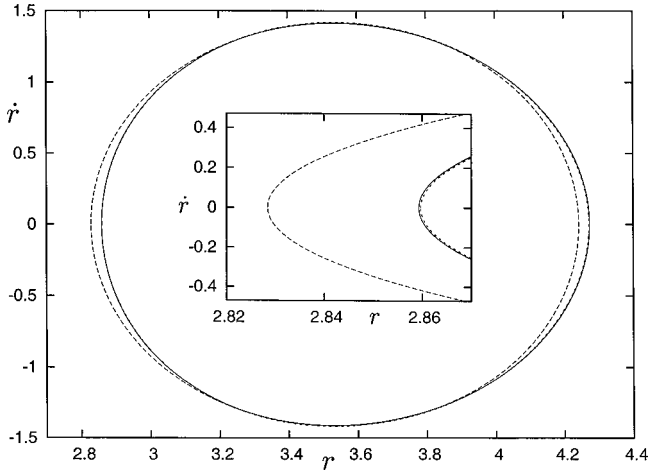

FIG. 14. The limit cycle $r_L(t)$ at $\eta = 5$ (full line) and two of its approximations. Long dashes: two-harmonics approximation $r_L^{(2)}(t)$. Short dashes: three-harmonics approximation $r_L^{(3)}(t)$. Inset: magnification of the limit cycles in the vicinity of $r = 2.85$.

$$2A_1^2 + 8A_2^2 = 1, \quad 2A_0A_1 + 5A_1A_2 = -\eta, \quad 8A_0A_2 + A_1^2 = 0. \tag{A4}$$

This system of equations is easily solved for A_1. Defining $x = A_1^2$ we obtain the cubic equation

$$144x^3 - 120x^2 + (25 + 16\eta^2)x - 8\eta^2 = 0. \tag{A5}$$

This equation is solved using Cardan's resolution formulas [37]. Following the procedure outlined in Ref. [53] we obtain

$$p = \frac{1}{27}\left[\eta^2 - \frac{25}{48}\right], \quad q = \frac{1}{81}\left[\frac{125}{576} - \eta^2\right],$$

$$u = [-q + \sqrt{p^3 + q^2}]^{1/3}, \quad v = -\frac{p}{u}, \quad x = u + v + \frac{5}{18},$$

$$A_0 = \frac{x}{\sqrt{8 - 16x}}, \quad A_1 = -\sqrt{x}, \quad A_2 = -\sqrt{\frac{1 - 2x}{8}}. \tag{A6}$$

Since $p^3 + q^2 > 0$ for $\eta \geqslant 3$, Eq. (A5) has only one real solution [37,53] and therefore Eq. (A6) is the only solution of Eq. (A5) of interest in the present context. Using Eq. (A6) in Eq. (A3) we obtain an explicit analytical result for $r_L^{(3)}(t)$ (short dashes in Fig. 14), which is almost indistinguishable from $r_L(t)$ on the scale of Fig. 14. The inset in Fig. 14 shows a magnification of the limit cycles in the vicinity of $r = 2.85$. The inset shows that even under strong magnification there is hardly any difference between $r_L(t)$ and $r_L^{(3)}(t)$. In fact, at $\eta = 5$, the relative error $|[r_L^{(3)}(t) - r_L(t)]/r_L(t)| < 7 \times 10^{-4}$ for all t and $|[\dot{r}_L^{(3)}(t) - \dot{r}_L(t)]/\dot{r}_L^{(\max)}| < 6 \times 10^{-3}$ for all t, where $\dot{r}_L^{(\max)} = \max_t |\dot{r}_L(t)|$. The error of the velocities is normalized to the maximum velocity since $\dot{r}_L(t) = 0$ at the turning points of the limit cycle.

[1] P. K. Ghosh, *Ion Traps* (Clarendon Press, Oxford, 1995).
[2] W. Paul, Rev. Mod. Phys. **62**, 531 (1990).
[3] W. Paul, W. Osberghaus, and E. Fischer, Forschungsber. Wirtsch.-Verkehrminist. Nordrhein-Westfalen **415**, 1 (1958).
[4] S. Hacyan and R. Jauregui, J. Opt. B: Quantum Semiclassical Opt. **5**, 138 (2003).
[5] V. I. Savichev and R. Blümel, Phys. Lett. A **309**, 211 (2003).
[6] M. Keller, B. Lange, K. Hayasaka, W. Lange, and H. Walther, J. Phys. B **36**, 613 (2003).
[7] U. Tanaka, S. Bize, C. E. Tanner, R. E. Drullinger, S. A. Diddams, L. Hollberg, W. M. Itano, D. J. Wineland, and J. C. Bergquist, J. Phys. B **36**, 545 (2003).
[8] M. Eichenseer, A. Yu. Nevsky, Ch. Schwedes, J. von Zanthier, and H. Walther, J. Phys. B **36**, 553 (2003).
[9] S. Gulde, H. Haffner, M. Riebe, G. Lancaster, C. Becher, J. Eschner, F. Schmidt-Kaler, I. L. Chuang, and R. Blatt, Philos. Trans. R. Soc. London, Ser. A **361**, 1363 (2003).
[10] D. Leibfried, B. DeMarco, V. Meyer, M. Rowe, A. Ben-Kish, M. Barrett, J. Britton, J. Hughes, W. M. Itano, B. M. Jelenković, C. Langer, D. Lucas, T. Rosenband, and D. J. Wineland, J. Phys. B **36**, 599 (2003).
[11] R. Blümel, Phys. Rev. A **51**, R30 (1995).
[12] R. Blümel, Appl. Phys. B: Lasers Opt. **60**, 119 (1995).
[13] E. Peik and J. Fletcher, J. Appl. Phys. **82**, 5283 (1997).
[14] R. Blümel, E. Bonneville, and A. Carmichael, Phys. Rev. E **57**, 1511 (1998).
[15] R. J. Cook, D. G. Shankland, and A. L. Wells, Phys. Rev. A **31**, 564 (1985).
[16] L. S. Brown, Phys. Rev. Lett. **66**, 527 (1991).
[17] J. M. Greene, R. S. MacKay, F. Vivaldi, and M. J. Feigenbaum, Physica D **3**, 468 (1981).
[18] K. R. Meyer, Trans. Am. Math. Soc. **149**, 95 (1970).
[19] I. Garrick-Bethell, Senior Thesis, Wesleyan University, 2002.
[20] I. Garrick-Bethell and R. Blümel, Phys. Rev. A **68**, 031404(R) (2003).
[21] W. Paul and F. von Busch, Z. Phys. **164**, 588 (1961).
[22] R. Alheit, S. Kleineidam, F. Vedel, M. Vedel, and G. Werth, Int. J. Mass Spectrom. Ion Processes **154**, 155 (1996).
[23] K. H. Kingdon, Phys. Rev. **21**, 408 (1923).
[24] R. R. Lewis, J. Appl. Phys. **53**, 3975 (1982).
[25] T. Biewer, D. Alexander, S. Robertson, and B. Walch, Am. J. Phys. **62**, 821 (1994).
[26] D. P. Moehs and D. A. Church, Phys. Rev. A **59**, 1884 (1999).
[27] R. Blümel, Phys. Scr., T **59**, 126 (1995); **59**, 369 (1995).
[28] M. C. Gutzwiller, *Chaos in Classical and Quantum Mechanics* (Springer, New York, 1990).
[29] R. E. Bahr, Diplomarbeit, Physikalisches Institut der Universität Freiburg, 1969.
[30] E. Behre, Zulassungsarbeit, Physikalisches Institut der Universität Freiburg, 1972 (unpublished).
[31] E. Teloy (private communication).
[32] S. J. Linz, Phys. Rev. A **52**, 4282 (1995).
[33] N. Yu and H. Dehmelt, in *Trapped Charged Particles and Fundamental Physics*, edited by D. H. E. Dubin and D. Schneider, AIP Conf. Proc. No 457 (AIP, Woodbury, NY, 1999).
[34] J. Guggenheimer and P. Holmes, *Nonlinear Oscillations, Dynamical Systems, and Bifurcations of Vector Fields* (Springer, New York, 1983).
[35] H. G. Dehmelt, Adv. At. Mol. Phys. **3**, 53 (1967).
[36] H. Dehmelt, Rev. Mod. Phys. **62**, 525 (1990).
[37] M. Abramowitz and I. A. Stegun, *Handbook of Mathematical Functions* (National Bureau of Standards, Washington, DC, 1964).
[38] I. S. Gradshteyn and I. M. Ryzhik, *Table of Integrals, Series and Products*, 5th ed., edited by A. Jeffrey (Academic Press, Boston, 1994).
[39] N. Saito, H. Hirooka, J. Ford, F. Vivaldi, and G. H. Walker, Physica D **5**, 273 (1982).
[40] H. E. Lehtihet and B. N. Miller, Physica D **21**, 93 (1986).
[41] V. I. Arnold, *Mathematical Methods of Classical Mechanics*, 2nd ed. (Springer, New York, 1989).
[42] A. J. Lichtenberg and M. A. Lieberman, *Regular and Stochastic Motion* (Springer, New York, 1983).
[43] J. A. Hoffnagle and R. G. Brewer, Appl. Phys. B: Lasers Opt. **60**, 113 (1995).
[44] M. G. Moore and R. Blümel, Phys. Rev. A **50**, R4453 (1994).
[45] J. W. Emmert, M. Moore, and R. Blümel, Phys. Rev. A **48**, R1757 (1993).
[46] R. Blümel, J. M. Chen, E. Peik, W. Quint, W. Schleich, Y. R. Shen, and H. Walther, Nature (London) **334**, 309 (1988).
[47] J. Hoffnagle, R. G. DeVoe, L. Reyna, and R. G. Brewer, Phys. Rev. Lett. **61**, 255 (1988).
[48] C. F. F. Karney, Physica D **8**, 360 (1983).
[49] J. D. Meiss and E. Ott, Phys. Rev. Lett. **55**, 2741 (1985).
[50] L. D. Landau and E. M. Lifshitz, *Mechanics* (Pergamon, Oxford, 1960).
[51] C. F. Hillermeier, R. Blümel, and U. Smilansky, Phys. Rev. A **45**, 3486 (1992).
[52] R. Blümel, in *Quantum Chaos*, Proceedings of the International School of Physics "Enrico Fermi," Course CXIX, edited by G. Casati, I. Guarneri and U. Smilansky (North-Holland, Amsterdam, 1993), pp. 385–398.
[53] G. Arnold, in *Formeln der Mathematik*, edited by H. Netz (Carl Hanser Verlag, Munich, 1975).